Determination of the Rate Constant for the Radical−Radical Reaction $CN(X^2\Sigma^+)$ + $OH(X^2\Pi)$ at 292 K

Brian K. Decker[†] **and R. Glen Macdonald***

Argonne National Laboratory, Chemistry Division, 9700 South Cass Avenue, Argonne, Illinois 60439-4831

Received: May 8, 2003; In Final Form: August 14, 2003

The rate constant for the reaction of the cyano radical, $CN(X^2\Sigma)$, with the hydroxyl radical, $OH(X^2\Pi)$, has been measured to be $(1.4 \pm 0.48) \times 10^{-10}$ cm^3 molecule^{-1} s^{-1} at a temperature of 292 ± 2 K. The error estimate includes both systematic and random error at the level of one standard deviation. The measurements were carried out by simultaneously monitoring the temporal dependencies of the CN and OH radical concentrations on the same photolytic laser pulse that created the transient species. The rate constant was determined by two independent methods of data analysis: one based on the simulation of CN and OH concentration profiles using a detailed kinetic mechanism and the other based on a new integrated-profiles analysis (*Int. J. Chem. Kinet.* **1998**, *30,* 47).

I. Introduction

There is an increasing interest in reducing NO_X emissions from combustion sources, particularly from fixed power generation stations. Many strategies have been proposed to carry out this reduction,[1] including combustion modification, reburn technologies, and selective noncatalytic reduction of NO, SNCR processes. The SNCR technologies achieve NO_X reduction by the addition of various reagents to the post combustion gases to chemically remove NO_X. The three main SNCR strategies, employing the indicated postcombustion gases, are the thermal De-NO_X process (NH_3), the RAPRENO$_X$ process, $(HOCN)_3$, and the NO_XOUT process, $(NH)_2CO$. In all three cases, the understanding of the reactions leading to NO_X reduction is not complete.[2]

There are three main mechanisms for NO_X production in combustion systems: the Zeldovich mechanism, initiated at high temperatures by the $O(^3P) + N_2$ reaction; the Fenimore or prompt NO_X mechanism, arising from the reaction of N_2 with simple hydrocarbon radicals such as CH and $^1CH_2$; and fuel-fixed nitrogen sources, initiated by the oxidation of HCN.[1] The Zeldovich mechanism involves only a relatively few elementary reaction steps and has been well characterized.[1] The other major mechanisms of NO_X generation are much more complex, involving many reactions and chemical species, and as a result, have been more difficult to describe.[3]

The CN radical is an important intermediate in the chemistry of both NO_X generation and reduction processes. It is produced directly in the Fenimore and fuel-fixed nitrogen oxidation chemistry and plays an important role in the SNCR chemistry, being an active N atom carrier. The CN + OH reaction is an important process in the CN radical chemistry cycle. Depending on the product channels, it can be a terminating reaction, leading to a reduction of the radical pool, or it can lead to either the NCO or NH chemical pathways for NO_X reduction or production. The high-temperature shock tube measurements of Wooldridge et al.[4] are the only previous direct experimental results on this reaction.

The ground-state reaction of the cyano radical, $CN(X^2\Sigma)$, with the hydroxyl radical, $OH(^2\Pi)$. has five exothermic product channels, given by

$$CN(X^2\Sigma) + OH(^2\Pi) \rightarrow HNC(X^1\Sigma) + O(^3P) \quad \Delta H_f^0(0) = -26.7 \pm 10.4 \text{ kJ mol}^{-1} \quad \text{(R1a)}$$

$$\rightarrow NH(a^1\Delta) + CO(X^1\Sigma) \quad \Delta H_f^0(0) = -74.4 \pm 1.3 \text{ kJ mol}^{-1} \quad \text{(R1b)}$$

$$\rightarrow HCN(X^1\Sigma) + O(^3P) \quad \Delta H_f^0(0) = -88.7 \pm 6.2 \text{ kJ mol}^{-1} \quad \text{(R1c)}$$

$$\rightarrow NCO(X^2\Pi) + H(^2S) \quad \Delta H_f^0(0) = -129.5 \pm 6.5 \text{ kJ mol}^{-1} \quad \text{(R1d)}$$

$$\rightarrow NH(X^3\Sigma) + CO(X^1\Sigma) \quad \Delta H_f^0(0) = -225.8 \pm 1.3 \text{ kJ mol}^{-1} \quad \text{(R1e)}$$

where the $\Delta H_f^0(0)$'s, in kJ mol^{-1}, of the transient molecules were taken as follows: CN = 432 ± 4,[5] OH = 36.9 ± 0.4,[6] HNC = 195.4 ± 4.2,[7] $NH(a^1\Delta)$ = 508.3 ± 1.3,[8] $NH(X^3\Sigma)$ = 356.9 ± 1.3,[9] NCO = 129.5 ± 2.5.[5] The CN radical was monitored using rovibrational transitions of the $CN(A^2\Pi) \leftarrow (X^2\Sigma)$ (2,0) band near 790 nm, and the OH radical was monitored using the $P_{1e}(5.5)$ rotational transition of the vibrational fundamental. In related experiments, the CN radical and one of the infrared absorbing species in each of the five product channels were also monitored simultaneously, and the product branching ratios were determined. The present work presents the determination of the room-temperature rate constant for this radical−radical reaction.

The determination of a second-order rate coefficient[10] between a stable molecule and a transient species can be determined by measuring the decay rate of the transient as a function of the concentration of the stable molecule. As long as the transient species has a much smaller concentration than the stable molecule, a plot of its decay rate against the concentration of the stable molecule is linear with a slope equal to the rate

* Corresponding author. E-mail: rgmacdonald@anl.gov.
[†] Present address: Physical Sciences, Inc., 20 New England Business Center, Andover, MA 01810.

10.1021/jp030591q CCC: $25.00
Published on Web 10/03/2003

coefficient. Under these pseudo-first-order conditions, the concentration of the transient species does not need to be determined. On the other hand, radical−radical reactions pose a particular experimental challenge. In general, the time dependence of the concentration of both species must be followed to determine second-order rate coefficients between them. Under some circumstances, it is possible to achieve pseudo-first-order conditions with a large excess of one transient species over the other. However, self-reaction by the species in excess restricts the implementation of this strategy. In the current work, this limitation was circumvented by simultaneously monitoring the time dependence of the two radicals following their production using 193 nm excimer laser photolysis of appropriate precursors.

In addition, the rate constant for reaction R1, k_{R1}, was determined by two different methods. The first method was based on the integrated-profiles method suggested by Yamasaki and co-workers.[11,12] This method uses a multilinear regression analysis of the experimental concentration profiles to determine the first- and second-order rate constants involving the CN radical. In the second method, a detailed kinetic model was developed to describe the chemistry occurring in the CN + OH reaction system. The value of k_{R1} was determined by minimizing the sum of the squares of the residuals between the model and experimental CN concentration profiles as a function of k_{R1}. Within experimental scatter, both procedures gave the same k_{R1}.

II. Experimental Section

The experimental apparatus has been described in detail,[13] but for completeness, a brief description will be given here. The reaction vessel consisted of a rectangular stainless steel chamber containing a Teflon box with interior dimensions of $100 \times 100 \times 5$ cm. The reaction vessel was evacuated to less than 5.0×10^{-6} Torr and had a leak rate of about 5×10^{-4} Torr min^{-1}. During the experiment, the reagent gases were admitted into the reaction vessel from separate vacuum systems through calibrated MKS mass-flow meters and were continuously pumped by a liquid-nitrogen-trapped mechanical pump. The partial pressures of the reagents were determined from the total pressure and their measured flow rates. The gases used were Ar (AGA Gas, 99.995% pure), N_2O (AGA Gas, 99.998% pure), and $(CN)_2$ (Matheson and Spectra Gases, 98.5% pure). Generally, the gases were used directly as supplied by the manufacturer except that the $(CN)_2$ was stored in a 20 L glass bulb and occasionally pumped under liquid-nitrogen. In some experiments, the Ar was passed through an AGA supplied O_2 removal filter.

A known flow of H_2O vapor was admitted to the reaction vessel through a saturated-bubbler system. The partial pressure of H_2O in the bubbler was controlled by varying the temperature of the water reservoir using a Neslab RTE-111 water-bath recirculator. Distilled H_2O was added to the bubbler system by vacuum distillation following several freeze−thaw cycles. Great care was taken to ensure that air was removed from the bubbler system before each experiment.

The photolysis laser was a Lambda-Physik Compex 205 excimer laser operating at a wavelength of 193 nm with a nominal fluence of 9−12 mJ cm^{-2} at the entrance window to the reaction vessel. The repetition rate of the laser was usually 2 Hz but was varied between 1 and 5 Hz with no apparent influence on the measured rate constant. The excimer laser was always operated in the constant energy mode, and except for minor pulse-to-pulse fluctuations, the laser intensity was constant over an experimental run.

An Environmental Optical Sensor model 2010-EU tunable-external-cavity diode laser, operating around 790 nm, was used to monitor CN on the A $^2\Pi \leftarrow$ X $^2\Sigma^+$ (2,0) band near 790 nm. A Burleigh Model 20 single-mode color center laser, operating between 2.6 and 3.3 μm was used to monitor OH on the X $^2\Pi_{3/2,1/2}$ (1) ← (0) fundamental vibrational band. Both probe laser beams were spatially overlapped by dichroic mirrors and multipassed through the photolysis region using a White-cell arrangement. The optical path length was defined by the number of passes through the photolysis volume and the distance between the UV−IR dichroic mirror that spatially overlapped the photolysis and probe laser beams and a Brewster's angle ZnS plate that absorbed the UV laser radiation before striking the opposite White-cell mirror. After passage through the photolysis region, the two probe laser beams were separated by another dichroic mirror and detected by the appropriate detectors: the near-IR laser by a Si PIN diode and the IR by a liquid-nitrogen cooled InSb detector. This arrangement allowed the simultaneous detection of the CN(v=0) radical and an infrared absorbing species, such as OH, on the same photolysis laser pulse.

For the detection of an infrared absorbing species, a major source of noise was intensity fluctuations of the infrared-probe laser radiation. This noise was suppressed in two ways. First, the infrared beam was split into two beams, a reference and a signal beam, whose intensities were monitored by separate liquid-nitrogen cooled InSb detectors. The reference detector output was used in the feedback circuit of an optical modulator (ConOptics), and hence, regulated the intensity of the color center pump Kr^+ laser in accordance to fluctuations in the infrared laser intensity. Second, balanced signals from the reference and signal detectors were input into a fast differential amplifier, further reducing common-mode noise.

The simultaneous time-resolved transient absorption signals for CN and OH were recorded and signal averaged using a LeCroy model 9410 digital oscilloscope, operating in the DC mode. Between 100 and 500 laser pulses were acquired for a signal-averaged profile. A background signal due to thermal lensing and refractive index changes, induced in the optical elements that were exposed to the UV photolysis radiation, was evident on the much smaller infrared signal. This background was removed from the signal channel by recording a second trace with the infrared laser detuned about 0.015 cm^{-1} from the absorption maximum and subtracting the background from the signal profile.

The experimental absorption profiles were converted into concentration profiles using the Beer−Lambert law. The absorbance of species X, $A_X(\nu)$, where ν is the probe laser frequency, is related to the concentration of X, [X], where the square brackets indicate concentration, by[14]

$$A_X(\nu) = \ln(I_0(\nu)/I(\nu)) = l\sigma(\nu)[X] \qquad \text{(E1)}$$

where $I_0(\nu)$ is the incident laser intensity, $I(\nu)$ is the transmitted laser intensity, l is the path length, and $\sigma(\nu)$ is the absorption cross section.

For the CN monitoring laser, I_0 was determined directly from the DC recorded transient absorption signal using the pretrigger delay feature of the digital oscilloscope. For the OH monitoring laser, I_0 was monitored by a box car that was triggered 0.1 ms prior to the excimer laser trigger pulse and was held virtually constant by the optical feedback system. Uncertainty in the determination of I_0 was quite small, less than ±1%, for each laser system.

As outlined in previous work,[15] $\sigma(\nu)$ is given by the product of the line strength of the probed transition and a line shape function, taken to be a Doppler profile. An absorption measurement actually measures the degeneracy-weighted difference in population between the states connected by the radiative transition so the population in the upper state must be small to obtain an accurate description of the lower state population. This will be further illustrated in section III.A. The bandwidth of both probe laser sources was much narrower than the Doppler width of all probed species, so that the probe laser frequency could be tuned to the peak of the absorption feature. Uncertainty in determining the peak of an absorption feature results in an uncertainty in determining the concentration of the absorber. The determination of the peak in an absorption feature was aided by maximizing the averaged output from two Stanford SR-250 box car modules that monitored both transient absorption signals.

III. Results

A. Radical Generation. The photolytic generation of radicals from stable molecules usually results in the generation of two transient species if a single chemical bond is cleaved in the process, and more, if other photochemical channels are possible. Thus, photolysis results in a radical pool with equal initial concentrations of at least two transient species. The radical precursor is of course chosen so that the chemistry of the desired transient species dominates that of its coproduct. In the current experiment, this situation was avoided by generating the CN and OH radicals in a manner that minimized the production of other transients. The following series of reactions describes the initial production of CN and OH radicals:

$$(CN)_2 \xrightarrow{193\ nm} 2CN \quad (1)$$

$$N_2O \xrightarrow{193\ nm} N_2 + O(^1D) \quad (2)$$

$$O(^1D) + H_2O \rightarrow 2OH \quad (3a)$$

$$\rightarrow H_2 + O_2 \quad (3b)$$

$$\rightarrow O(^3P) + H_2O \quad (3c)$$

$$O(^1D) + N_2O \rightarrow N_2 + O_2 \quad (4a)$$

$$\rightarrow 2\ NO \quad (4b)$$

$$O(^1D) + Ar \rightarrow O(^3P) + Ar \quad (5)$$

$$O(^1D) + (CN)_2 \rightarrow CN + NCO \quad (6)$$

$$CN + OH \rightarrow \text{product channels} \quad (R1)$$

The electronic deactivation rate constant of $O(^1D)$ by N_2O has not been measured but is likely small. Also, there is no experimental information on reaction 6, but it was included in the mechanism with an assigned value of 1×10^{-11} cm^3 $molecules^{-1}$ $s.^{-1}$ The combined concentration of $[N_2O]$ and $[H_2O]$ was always at least 10 times greater than the $[(CN)_2]$ so that, even if k_6 was gas kinetic, this process would contribute less than 10% to the removal of $O(^1D)$.

The complete reaction mechanism describing the chemistry of the CN + OH system will be described in another work, but for the present purpose, the reactions involving $O(^1D)$, CN, and OH are summarized in Table 1, along with the corresponding rate constants, at 292 K.[16−28]

TABLE 1: Summary of the Reactions and Rate Constants Involving the Production and Removal of CN and OH Radicals

no.	reactants	products	k^a	ref
3a	$O(^1D) + H_2O$	$\rightarrow OH + OH$	2.02×10^{-10}	16
3b		$\rightarrow H_2 + O_2$	1.20×10^{-12}	16
3c		$\rightarrow O(^3P) + H_2O$	9.9×10^{-12}	16
4a	$O(^1D) + N_2O$	$\rightarrow NO + NO$	7.2×10^{-11}	16
4b		$\rightarrow N_2 + O_2$	4.4×10^{-11}	16
5	$O(^1D) + Ar$	$\rightarrow O(^3P) + Ar$	5.00×10^{-13}	17
6	$O(^1D) + (CN)_2$	$\rightarrow CN + NCO$	1.0×10^{-11}	guess
R1	$CN + OH$	$\rightarrow$products	varied	this work
8	$CN + CN + M$ Ar=N_2/1.0/N_2O=H_2O/2	$\rightarrow (CN)_2 + M$	3.2×10^{-29}	18
9	$CN + O$	$\rightarrow CO + N$	3.7×10^{-11}	19
10	$CN + H_2$	$\rightarrow HCN + H$	2.41×10^{-14}	20
11a	$CN + NH$	$\rightarrow HCN + N$	5.0×10^{-11} adjusted	guess
11b		$\rightarrow HNC + N$	5.0×10^{-11} adjusted	guess
12a	$CN + O_2$	$\rightarrow NCO + O$	1.8×10^{-11}	16, 21
12b		$\rightarrow CO + NO$	6.1×10^{-12}	
13	$CN + H_2O$	$\rightarrow OH + HCN$	3.64×10^{-17}	22
14	$CN + N_2O$	$\rightarrow NCN + O$	8.38×10^{-18}	23
15	$OH + H + M$ Ar/1.0/N_2O/2.7/H_2O/16	$\rightarrow H_2O + M$	2.7×10^{-31}	24
		$\rightarrow O(^3P) + H_2$		24
16	$OH + N$	$\rightarrow H + NO$	5.1×10^{-11}	25
17	$OH + O$	$\rightarrow H + O_2$	4.2×10^{-11}	25
18	$OH + CO$	$\rightarrow H + CO_2$	1.2×10^{-13}	24
19	$OH + H_2$	$\rightarrow H + H_2O$	5.9×10^{-15}	16
20a	$OH + NH$	$\rightarrow H + HNO$	3.0×10^{-11} adjusted	this work
20b		$\rightarrow N + H_2O$	3.0×10^{-12}	25
21	$OH + NO + M$ Ar/1.0/N O/2.0/H_2O/20.0	$\rightarrow HONO + M$	3.5×10^{-31}	24
22	$OH + OH$	$\rightarrow O + H_2O$	1.45×10^{-12}	27
23	$OH + OH + M$ Ar/1.0/N_2O/1.0/H_2O/5.8	$\rightarrow H_2O_2 + M$	6.9×10^{-31}	28
24	$OH + HO_2$	$\rightarrow O_2 + H_2O$	1.1×10^{-10}	16
25a	$OH + (CN)_2$	$\rightarrow NCO + HCN$	varied	this work
25b		$\rightarrow NCO + HNC$	varied	
26	$OH + H_2O_2$	$\rightarrow HO_2 + H_2O$	1.7×10^{-12}	16

[a] Second-order rate constants cm^3 $molecule^{-1}$ s^{-1}, third-order rate constants cm^6 $molecule^{-2}$ s^{-1}. For recombination reactions the falloff region was accounted for using simplified parameters, k_0, k_∞, and F_c.[16]

The reactive species that are produced by the initial photolysis-induced chemistry are $O(^3P)$ and O_2. As can be seen from Table 1, these species have large reaction rate constants with CN, and their reactions with CN could potentially interfere with the determination of k_{R1}. However, under the conditions of the experiments, electronic quenching of $O(^1D)$ was much slower than the removal of $O(^1D)$ by reactions k_{3a} and k_4 so that the initial $[O(^3P)]$ was small. In addition, the initial $[O_2]$ produced by reactions 3b and 4a, was significantly less than the initial [OH] because k_{3a} is a factor of 3 greater than k_{4a} and the $[H_2O]$ was usually larger than $[N_2O]$. Thus, at least initially, the radical pool consisted primarily of CN and OH radicals, with the $[O_2]$ much smaller than the [OH].

The k_{R1} can be determined by two distinct methods and the results of these two determinations compared. The first method is based on the measured [CN] and [OH] temporal profiles whereas the second is based on the simulation of these profiles using a detailed chemical model of the reaction system. Fortunately, most reactions needed to describe the CN−OH system have been well characterized. The two different methods used to determine k_{R1} are described in the following sections.

The first 5×10^{-3} s of typical [CN] and [OH] temporal profiles are shown in Figures 1a,b, respectively. The measured

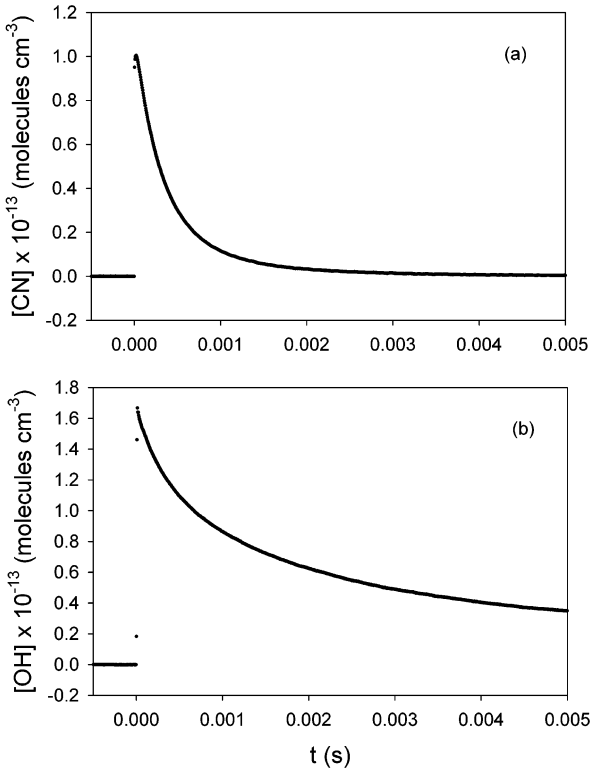

Figure 1. (a) First 5×10^{-3} s of a typical [CN(v=0)] temporal profile. The CN was monitored by the R_1(14.5) line of the ($A\ ^2\Pi \leftarrow X\ ^2\Sigma$) (2,0) band near 790 nm. The conditions of the experiment were [Ar] = 9.43×10^{16}, [H_2O] = 3.58×10^{16}, [N_2O] = 1.05×10^{16}, and [$(CN)_2$] = 2.19×10^{15} molecules cm^{-3}. (b). As in (a), except for an [OH(v=0)] temporal profile acquired on the same photolysis laser pulse as the [CN(v=0)] in (a). The [OH] was monitored using the P_{1e}(5.5) transition of the vibrational fundamental.

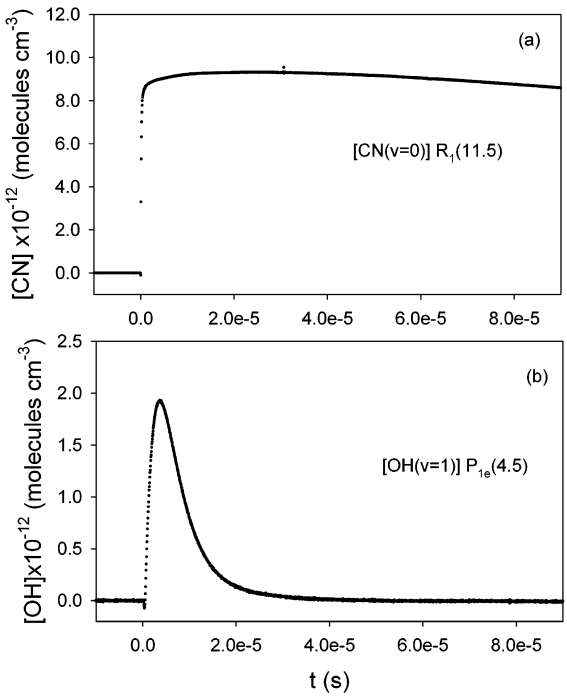

Figure 2. (a) Initial portion of a typical [CN(v=0)] temporal profile to show the effects of rotational and vibrational relaxation under conditions similar to Figure 1. The rapid rise and plateau region of the [CN] profile are attributed to rotational and vibrational relaxation, respectively. The conditions of the experiment were [Ar] = 1.11×10^{17}, [H_2O] = 1.53×10^{16}, [N_2O] = 1.01×10^{16}, and [$(CN)_2$] = 2.68×10^{15} molecules cm^{-3}. (b). Temporal profile for [OH(v=1)] showing the rapid vibrational relaxation of OH(v=1). As in Figure 1, both the CN(v=0) and OH(v=1) profiles were recorded on the same photolysis laser pulse.

temporal absorbance profiles were converted to concentration profiles for each species using known line strengths.[29−31] As noted previously, the absorption line shape for all the transitions was assumed to be Doppler. At the pressures of the experiment, 3−8 Torr, pressure broadening was estimated to reduce the peak absorption cross sections by a few percent for the highest pressure experiments, well within the scatter of the measurements.

Not only can photolysis generate multiple transient species but also the photolysis energy greater than the bond dissociation energy is partitioned into translational and internal energy of the products. The production of internally excited CN and OH products is illustrated in Figures 2a,b, respectively. The 193 nm photolysis of $(CN)_2$ produces CN radicals that are characterized by an average translational temperature of 3850 K, a rotational temperature of 2200 K, and a vibrational population distribution with 13% in the CN(v=1) level.[32] At the pressures used in the present experiments, rapid quenching of translation and rotation occurred within the first microseconds, as indicated by the initial rapid rise in the CN(J=11.5) population shown in Figure 2a. Transitions from CN(v=1) were outside the tuning range of the diode laser; however, the slow rise in [CN(v=0,J=11.5)] up to about 40 μs was attributed to the production of CN(v=0) from vibrational relaxation out of CN(v=1). The high partial pressures of H_2O and N_2O are likely responsible for the rapid vibrational relaxation of CN(v=1). Figure 2b shows the temporal profile for [OH(v=1,J=4.5] created in reaction 3a. The initial internal state distribution of OH, created in reaction 3a, has been investigated by several workers.[33,34] Again, both translation and internal degrees of freedom are excited, with the "new" OH bond receiving more of the internal energy. The initial OH vibrational state distribution was found to be 0.67:0.18:0.15 for v = 0, 1, and 2, respectively. As shown in Figure 2b, both rotational and vibrational relaxation of OH(v=1) occurred very rapidly. A small inversion between the quantum states connected by the OH(v=2) ← OH(v=1) P_{1e}(4.5) transition is indicated by the initial small negative signal; however, excited vibrational levels of OH were rapidly quenched. Note that the peak concentration in [OH(v=1)] in Figure 2b is only 10% of the peak [OH(v=0)] in Figure 1b and that the lifetime of OH(v=1) corresponds to only 5 data points in Figure 1b.

B. Direct Determination of k_{R1}. As suggested in the Introduction, the direct determination of radical−radical rate constants is relatively rare. The CN + OH reaction is a second-order process, and the time dependence of the concentration of both transient species was measured to determine k_{R1}.

These circumstances allowed for the determination of k_{R1} by direct integration of the experimental concentration profiles, following the integrated-profiles method suggested by Yamasaki, Watanabe, and co-workers.[11,12] As discussed in section III.A, the removal of CN is dominated by reaction with the OH radical. The kinetic model describing the reactions occurring in the CN and OH system will be discussed in detail in section III.C. Reactions involving CN with other species can be separated from reaction R1 and treated as a first-order loss process for CN. Thus, the time dependence of CN can be expressed by the following rate equation:

$$\frac{d[CN]}{dt} = -k_{R1}[OH][CN] - k_{first}[CN] \qquad (7)$$

TABLE 2: Summary of the Experimental Results for the Determination of k_{R1} by the Direct Integration of Profiles Method and the Comparison of the Simulation of the [CN] Profiles from a Detailed Kinetic Model of the Chemistry Occurring in the CN−OH System

				integrated-profile k_{first}^{CN} fixed		integrated-profile k_{first} varied		computer simulation [CN]	
P_T (Torr)	$[H_2O]/[N_2O]$	$10^{13}[OH]_0$[a]	$[OH]_0/[CN]_0$	$10^{10}k_{R1}$[b]	$10^{-2}k_{first}^{CN}$ t[c]	$10^{10}k_{R1}$[b]	$10^{-2}k_{first}$[c]	$10^{10}k_{R1}$[b]	$10^{10}\Delta k_{R1}$[e]
4.43	1.60	0.736	1.22	1.39	3.60	1.22	5.01	1.53	0.20
4.46	1.21	1.30	1.92	1.39	3.60	*(0.437)*[d]	*(14.0)*	1.36	0.16
4.35	3.42	1.65	1.62	1.60	3.00	1.46	5.87	1.47	0.17
4.38	2.63	2.01	1.91	1.45	3.37	1.34	5.16	1.45	0.15
4.72	0.731	2.45	3.04	1.49	5.00	1.31	8.85	1.49	0.18
4.68	1.11	2.74	3.32	1.20	3.00	*(0.479)*	*(21.3)*	1.27	0.10
7.43	1.125	3.90	3.00	1.18	7.05	0.998	12.3	1.20	0.10
3.00	3.53	0.728	2.00	1.60	2.25	1.51	2.84	1.45	0.25
3.27	0.840	2.21	4.59	1.32	3.00	*(0.078)*	*(27.9)*	1.46	0.20
4.22	1.52	1.40	2.31	1.54	3.30	1.43	4.86	1.56	0.15
5.93	4.21	1.95	1.70	1.56	5.16	1.67	4.13	1.55	0.15
4.68	1.12	2.72	4.33	1.37	3.00	*(1.01)*	*(12.4)*	1.33	0.10
4.04	0.419	1.30	1.29	1.53	2.90	*(0.611)*	*(10.9)*	1.30	0.15
5.99	0.990	1.50	0.943	1.59	5.50	1.21	9.94	1.35	0.25
			av	1.45		1.37		1.41	0.17
			std dev	±0.14		±0.20		±0.11	

[a] Concentration units molecules cm^{-3}. [b] Second-order rate constant units molecules cm^{-3} s^{-1}. [c] First-order rate constant units s^{-1}. [d] Values enclosed by brackets and in italics were neglected in determining k_{R1}. [e] Goodness-of-fit parameter estimate of the uncertainty in k_{R1} at the 68% level of confidence.

where k_{first} represents the sum of all pseudo-first-order loss processes for CN, i.e., reactions with other species not produced by laser photolysis and loss by diffusion. The integrated-profiles method simply evaluates [CN] at time t, $[CN]_t$, by direct numerical integration of eq 7, according to

$$[CN]_t - [CN]_0 = -k_{R1}\int_0^t [CN][OH]\,dt - k_{first}\int_0^t [CN]\,dt \quad (8)$$

The left-hand side of eq 8 can be evaluated directly form the observed [CN] profiles at a series of selected times, t, and compared to the right-hand side determined by direct integration of the appropriate experimental concentration profiles of CN and OH. The rate constants k_{R1} and k_{first} are determined by a multilinear regression analysis.

A useful feature of this analysis method is that the integration can start at any time, allowing for the thermalization of any initially excited internal energy. In principle, all pseudo-first-order and first-order reactions removing CN can be separated from the reaction between CN and OH. However, in practice, it was sometimes found that there was a strong correlation between k_{R1} and k_{first}. Thus, the multilinear analysis of eq 8 could produce k_{first} values that ranged over unreasonably large values, depending on the relative value of [OH]/[CN], with proportionately smaller values returned for k_{R1}. As the ratio [OH]/[CN] became larger, the CN decay profiles more closely approximated simple exponentials, resulting in the correlation between k_{R1} and k_{first}. As will be discussed in section III.C, the removal of CN was dominated by reaction with OH and background impurities.

To circumvent the correlation problem, two different methods were used to determine k_{R1} using eq 8. At the pressures used in the experiments, the first-order loss of species from the photolysis region due to diffusion was characterized by two diffusion time constants, arising from the rectangular geometry of the excimer laser beam. A discussion of this diffusional loss process has been given previously.[35] The two observable species, which were not removed by reactions, HCN or HNC, were generated on a long-time scale by reactions 25a and 25b, and the direct observation of the rate constants for loss by diffusion was not possible. However, the conditions of the current experiments were similar to other experiments carried out in the same apparatus,[35] and the largest diffusional rate constant for HCN, k_{diff}^{HCN}, was known from those experiments. The k_{diff}^{X}'s for other species X were inversely scaled to k_{diff}^{HCN} using the reduced mass of X and HCN with respect to the average mass of the gas mixture. As will be discussed in section III.C, k_{diff}^{OH} determined in this way was in agreement with k_{diff}^{OH} determined from model simulations of OH temporal profiles with no CN present (see Figure 3).

In the absence of N_2O, the first-order loss for CN was found to be a factor of 3−4 times larger than the calculated diffusional loss rate constant. This faster loss process was attributed to a reaction with a contaminate in the vacuum system, likely O_2. The background removal rate constant for CN was unaffected by evacuation of the reaction chamber using a diffusion pump, a mechanical pump or the addition of an O_2 removal filter to the Ar gas line. The Ar flow was generally at least a factor of 3 greater than the flow of any other gas. As noted in section III.B, the leak rate of the reaction chamber was about 0.5 mTorr min^{-1}, so a constant partial pressure of air of a few millitorr could account for the larger loss rate for CN. The k_{first}'s for CN were measured by replacing the N_2O flow by the same Ar flow, and are labeled k_{first}^{CN} in Table 2. These values were substituted into eq 8, and held fixed. The k_{R1} was determined by a least-squares analysis.

The summary of the results for the determination of k_{R1} by the integrated-profiles method and from the simulation of the [CN] profiles using a detailed-kinetic model is given in Table 2. The values for k_{R1} determined using the integrated-profiles method with k_{first}^{CN} fixed, as described in the last paragraph, are presented in column 5 of Table 2. The measured values for k_{first}^{CN} are given in column 6. The values for k_{R1} and k_{first} determined using the integrated-profiles method following a multilinear least-squares analysis are given in columns 7 and 8, respectively. If the analysis returned values of k_{first} that were unreasonably large (a factor of 3 greater than the measured k_{first}^{CN}), these values were neglected in the determination of k_{R1} but are enclosed in parentheses and written in italics in columns 7 and 8 for completeness. As noted previously, with increasing

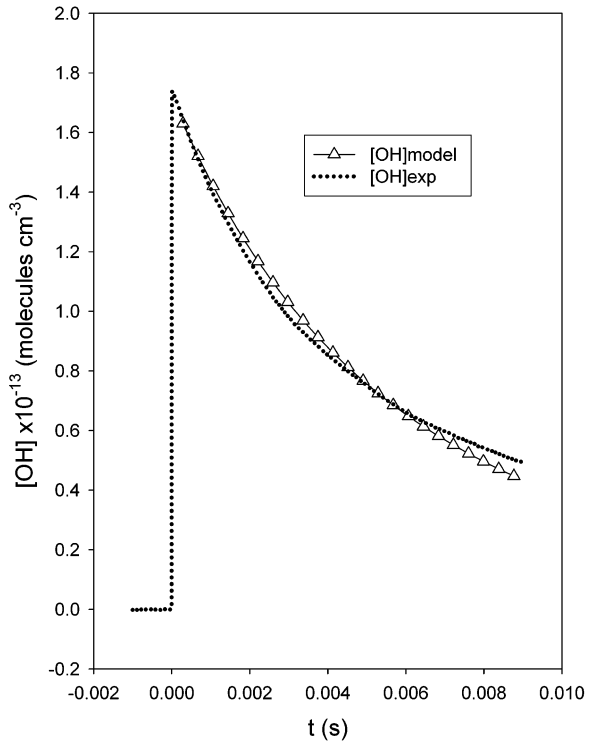

Figure 3. Decay of [OH(v=0)] obtained in the same experiment as Figure 1, but with no $(CN)_2$. The [OH] profile was simulated by a model calculation using the appropriate rate constants listed in Table 1 (see text). The conditions of the experiment were [Ar] = 9.43×10^{16}, [H_2O] = 3.58×10^{16}, and [N_2O] = 1.05×10^{16} molecules cm^{-3}.

[OH] compared to [CN], the kinetics of the CN decay became more pseudo-first-order like, and a strong correlation between k_{R1} and k_{first} developed, leading to unphysical results in the multiple-least-squares analysis. The second-to-last column in Table 2 gives the value of k_{R1} determined by simulating the CN temporal dependence using a detailed reaction mechanism to describe the system chemistry. The reactions involving the CN and OH radicals are listed in Table 1 and will be discussed in detail in the section III.C. As indicated by the last entry in columns 5, 7, and 9 in Table 2, the k_{R1}'s determined by the integrated-profiles method and the model simulations agreed, within the scatter of the measurements.

C. Model Determination of k_{R1}. The CN + OH system has been extensively investigated in this laboratory. In particular, the product branching ratios have been determined by monitoring a species, HNC, HCN, NH or NCO, from each of the possible product channels along with the CN radical. A complete description of these experiments and of the chemistry that occurs in the CN − OH system will be given in another work.[36] For the determination of k_{R1}, only the reactions removing or generating the CN and OH radicals are needed. These reactions are listed in Table 1. Fortunately, most of the reactions in Table 1 have been well studied, and their rate constants are well-known. The only reactions whose rate constants have not been well characterized are reactions (R1), (6), (11), (20), and (25).

For a complete description of the CN and OH chemistry, it is necessary to provide values for these unknown rate constants, k_6, k_{11}, k_{20}, and k_{25}. There is no information available on reaction 6, but it was included in the mechanism for completeness. Even if k_6 was gas kinetic the partial pressures of N_2O and H_2O were much larger than that for $(CN)_2$ and would dominate the removal processes for O^1D. There is no information available on reaction 11 so k_{11} was taken to be rapid in accordance with other H atom abstraction reactions by CN radicals from other H atom donors.[37] All the data were analyzed with k_{11} fixed at the value in Table 1. After a preliminary simulation of all the experimental [NH] profiles, the value of k_{20} given in the Table 1 was found to provide a good representation of the decaying portion of the NH profiles. For each experiment, the NH profile was then fit by varying k_{R1e} with k_{20} fixed. There are no direct experimental measurements of k_{20} near 300 K; however, several evaluations[24,38] estimate k_{20} to be 3×10^{-11} or 8×10^{-11} cm^3 molecule^{-1} s^{-1} with a large uncertainty. (The value of k_{20} determined in this work was in good agreement with an estimate provided by Miller and Bowman.[26]) There has been only one experimental measurement of k_{25}, and the experimental results suggested that the reaction occurred through a complicated three-body reaction sequence.[39] Unfortunately, both HCN and HNC were produced on a very long time scale in the CN + OH system, as well as by reaction (R1). After trial and error, it was concluded that that reaction 25 was likely responsible for this long time generation of HCN and HNC. Thus, the production of HCN and HNC from reactions (R1) and (25) could not be separated and k_{25a} and k_{25b} were varied along with the appropriate branching fraction to simulate the HCN and HNC profiles for each experiment. The average values of k_{25a} and k_{25b} resulting from these simulations were $(3.4 \pm 1.7) \times 10^{-15}$ and $(8.2 \pm 3.4) \times 10^{-16}$ cm^3 molecule^{-1} s^{-1}, respectively.

The initial $[O(^1D)]_0$ could not be determined experimentally; thus, in the computer simulations of the experimental profiles, $[O(^1D)]_0$ was varied until the calculated [OH] at 5×10^{-6} s was within ±2% of the experimental [OH] profile extrapolated back to $t = 0$. The initial $[CN]_0$ in the simulation was taken from the extrapolation of the experimental [CN] profile back to $t = 0$. No adjustments in the model rate constants depended on the experimental [OH] profile so that the agreement between the model predictions for the [OH] and the observed [OH] profile serve as a check on the appropriateness of the model chemistry.

The computer simulation determined k_{R1} by minimizing the sum of squares of the residuals between the calculated and experimental [CN] profile. This procedure also provided a goodness-of-fit parameter, Δk_{R1}. The last column in Table 2 gives an estimate of Δk_{R1} at the 68% confidence level.

As noted in section III.B, the first-order loss of CN was dominated by a background reaction and was accounted for in the model calculations assuming that CN was removed with the rate constant measured when the N_2O flow was replaced by the same Ar flow. The loss of species by diffusion from the photolysis region has been discussed in section III.B, and noted there, the values of k_{diff}^{HCN} were taken from previous experimental work carried out in this laboratory.[35]

In a reaction system involving many different species and reaction steps, it is important to be able to determine the influence of each reaction in the multistep process. The determination of k_{R1} requires that the concentration of both CN and OH be measured; thus, concentrations as well as rate constants play equally important roles in the evaluation of k_{R1}. A reaction contribution factor, RCF, analysis was used to determine the importance of a given reaction in the removal or production of each species.[1,3] For a reaction, X + I → products, having a rate constant k_{XI}, the reaction contribution factor for species X from species I at time t is given by

$$RCF_I^X = -k_{XI}[I][X] \qquad (9)$$

where RCF_I^X, [I], and [X] are evaluated at time, t, in the reaction mechanism. To a large extent, inspection of a plot of

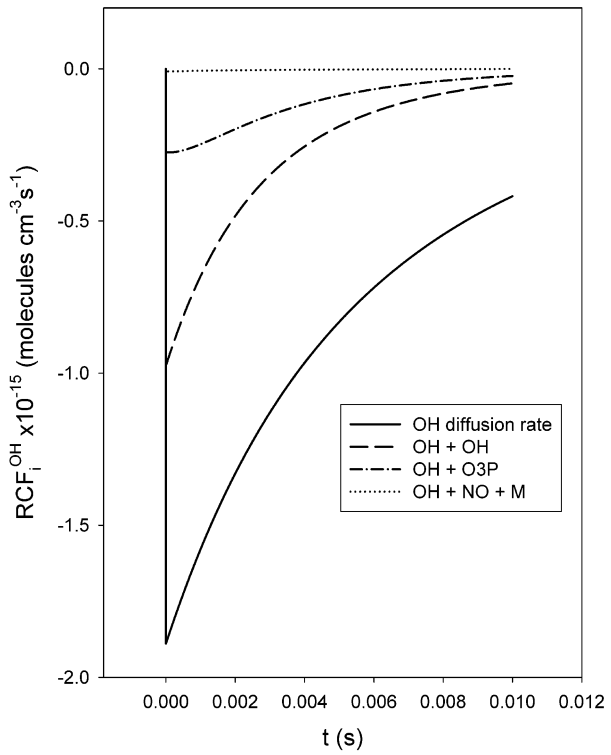

Figure 4. The RCF_i^{OH} for the model calculation shown in Figure 3. Only reactions with integrated RCF_i^{OH}'s greater than 1% of that for the self-removal of OH, reactions 22 and 23, are plotted. As discussed in the text, the removal of OH by diffusion dominated the removal by chemical reactions.

RCF_I^X vs time can be used to estimate the influence of a change in rate constant or reactant concentration on [X]. An important attribute of the RCF_I^X is that the integral of RCF_I^X from the initiation of the reaction to time, *t*, gives the net change in the concentration of species X due to reaction with I in that time interval.

A typical experimental and simulated [OH] profile obtained with the $(CN)_2$ flow turned off is shown in Figure 3. In the computer simulation, k_{diff}^{OH} was varied to obtain agreement between the simulated and experimental OH profiles. The simulated [OH] profile was calculated from the appropriate reactions listed in Table 1. The value of k_{diff}^{OH} found in the simulation, $k_{diff}^{OH} = 110\ s^{-1}$ was in good agreement with the value predicted by the use of $k_{diff}^{HCN} = 80\ s^{-1}$, measured under similar experimental conditions, as described in Sec III B.

Figure 4 shows an RCF analysis of the OH kinetics for the experimental run shown in Figure 3. In the absence of $(CN)_2$, the only removal processes for OH were reactions 17, 21, 22, and 23, and diffusion. After 10 ms, the integrated RCF_X^{OH}'s for these reactions gave the fractional removal of OH by these processes as 0.084, 0.023, 0.177, 0.016, and 0.685, respectively. Other reactions in Table 1 that could contribute to the OH kinetics had integrated RCF_X^{OH} values less than 1% of the integrated RCF_{OH}^{OH} value (reaction 2).

The k_{22} used in the profile simulations was taken from the recent measurement of Bedjanian et al.[27] The temperature dependence of k_{22} found by these workers was in good agreement with a detailed theoretical description[40] of reaction 22. A recent NASA evaluation[41] gives $k_{22} = 1.85 \times 10^{-12}$ cm^3 molecules^{-1} s^{-1}at 293 K, with an uncertainty of 40%. The large contribution of diffusion to the removal of OH made it impossible to differentiate between theses two values from the simulated profiles.

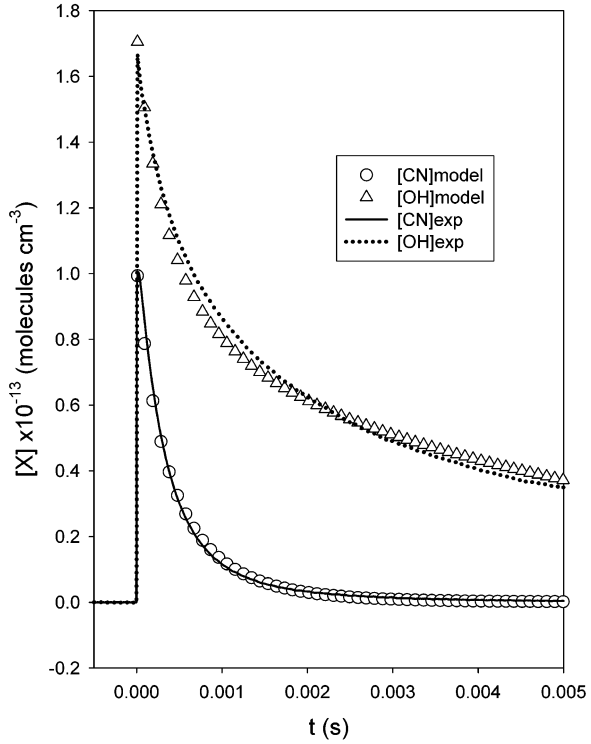

Figure 5. Complete experimental [CN] and [OH] profiles shown in Figure 1 are compared to the model simulation of these same profiles found by varying k_{R1} to minimized the sum of residues between the [CN] profiles. For this experiment, k_{R1} was found to be $(1.47 \pm 0.17) \times 10^{-10}$ cm^3 molecules^{-1} s.$^{-1}$ The error estimate is the goodness-of-fit estimate from the computer analysis. As can be seen from the figure, the agreement between the model predictions for both [CN] and [OH] temporal profiles is in good agreement with experiment. For clarity, the model profiles are shown for every 10th time step.

The computer simulations for the experimental [CN] and [OH] profiles shown in Figure 1 are presented in Figure 5. As discussed in section III.B, the removal of CN with the N_2O flow replaced by Ar was about 3 times the estimated loss by diffusion. This first-order loss, k_{first}^{CN} (Table 2), was included in the simulation. The computer analysis determined the best k_{R1} by minimizing the sum of squares of the residuals between the experimental and simulated [CN] profiles and returned an estimate of a goodness-of-fit parameter, $\pm\Delta k_{R1}$, at the 68% confidence level. As is evident from Figure 5, the agreement between the simulated and experimental [CN] profiles is excellent, resulting in a value of $(1.47 \pm 0.17) \times 10^{-10}$ cm^3 molecule^{-1} s^{-1} for k_{R1}. The results for the computer simulation of the [CN] and [OH] profiles are summarized in the last two columns of Table 2, showing k_{R1} and $\Delta k_{R1,}$ respectively. There is excellent agreement between the value of k_{R1} found from the two implementations of the integrated-profiles method and the computer simulation of the concentration profiles. As noted previously, the only variable in the computer simulations of the [OH] profile was the initial variation of $[O(^1D)]_0$. As is evident in Figure 5, there is also good agreement between the simulated and experimental [OH] profiles.

The RCF analysis of the computer simulation of the [CN] profile given in Figure 5 is shown in Figure 6. The RCF analysis is instructive, as it illustrates how the initial radical generation processes results in the initial dominance of the radical pool by the CN and OH species. In Figure 6a, RCF_{OH}^{CN} and RCF_{first}^{CN} are shown. The integrated RCF_X^{CN}'s show that reaction R1 and k_{first}^{CN} account for 79.5% and 16.6%, respectively, of the removal processes for the CN radical and only 3.9% is removed by

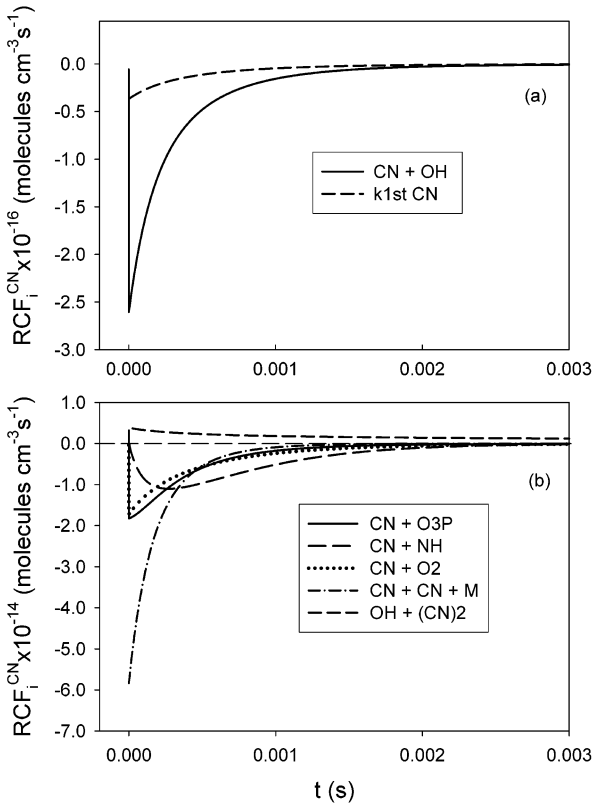

Figure 6. (a) RCF_X^{CN} analysis for the computer simulation shown in Figure 5. The two largest integrated RCF_X^{CN}'s were reaction with OH and the removal by a background reaction, k_{first}^{CN}. (b) RCF_X^{CN}'s with integrated values at least 1% of the integrated RCF_{OH}^{CN} value. Note, $RCF_{OH+(CN)_2}^{CN}$ is a production process.

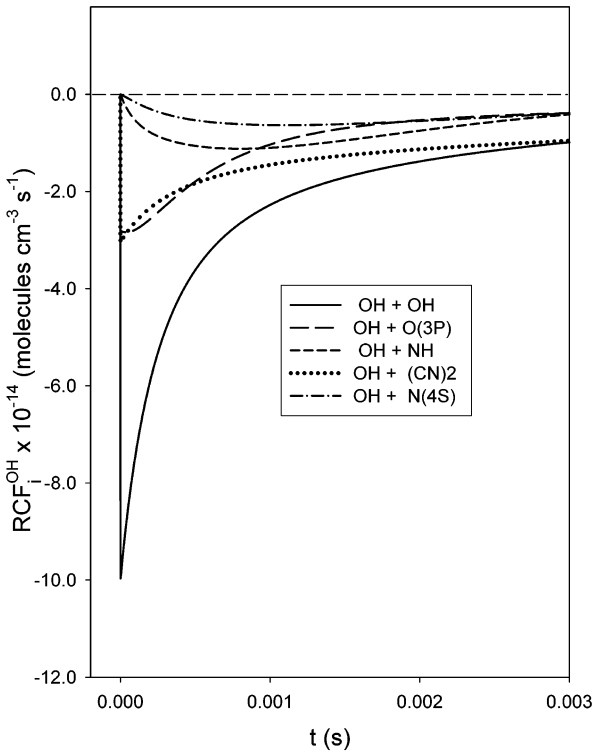

Figure 7. RCF_X^{OH} analysis for the computer simulation shown in Figure 5. For clarity, RCF_{diff}^{OH} is not shown but is similar to that shown in Figure 4. Only reactions that had integrated RCF_i^{OH} values greater than 1% of RCF_{CN}^{OH} are plotted.

reaction with other species in the system. Similar conclusions were found for all of the experimental conditions listed in Table 2. The dominance of reaction R1 as the major removal process for CN allowed the accurate determination of k_{R1} by the integrated-profile method presented in section III.B and summarized in Table 2.

Figure 7 shows the RCF analysis of the computer simulation of the [OH] profile in Figure 5. Only the reactions that had integrated RCF_X^{OH} values greater than 1% of the RCF_{CN}^{OH} value are shown in Figure 7. Under the experimental conditions of Figure 5, the time interval during which the [CN] was greater than 0 was 3 ms, and over this time frame, the removal of OH was dominated by reaction with CN. For example, the four largest removal processes and their integrated RCF_{CN}^{OH} removal fractions during this interval were $RCF_{CN}^{OH} = 0.679$, $RCF_{diff}^{OH} = 0.166$, $RCF_{OH}^{O} = 0.0607$, and $RCF_{(CN)2}^{OH} = 0.036$, respectively. A comparison of Figures 4 and 7 shows that the OH chemistry is considerably different when CN is present, in the former case dominated by diffusion losses and in the latter by reaction with CN. Similar behavior was found under the wide variety of experimental conditions shown in Table 2.

IV. Discussion.

A. Error Analysis. As noted previously, the determination of k_{R1} requires the measurement of both [CN] and [OH]. Uncertainty in the determination of the absorption coefficients for each transient species leads directly to a corresponding uncertainty in their respective concentrations, as suggested by eq E1. For the CN radical a variety of spectroscopic transitions in the $A^2\Pi \leftarrow X^2\Sigma$ (2,0) band were used in the course of this work. The line strengths of these transitions were taken from the theoretical calculations of Knowles et al.[29] and the Hönl London factors of Earls.[42] The uncertainty in these line strength values was taken as the theoretical estimate of ±5%. The theoretical line strength values are within 3% of a recent experimental measurement;[30] however, the experimental determination had a random error of ±13%, much larger than the estimated uncertainty in the theoretical calculation. The Doppler widths of the near-infrared CN transitions are a factor of 3.5 times those of OH and will not be influenced by pressure broadening at the low pressures used in the present experiments. The OH radical was monitored using the $P_{1e}(5.5)$ or the $P_{1f}(5.5)$ lines of the vibrational fundamental transition. The line strength for this transition was taken from the experimental and theoretical work of Nelson et al.[31] Although the line strength is based on recent calculations and experimental measurements, there is still a relatively large uncertainty of ±10% associated with its determination due to the strong vibrational−rotational interactions in the OH radical.[43] As is evident from Table 1, most of the experiments were carried out at a total pressure around 4 Torr with Ar comprising over 50% of the gas mixture. No data are available on pressure broadening parameters for the OH vibrational fundamental[43] by Ar, N_2O, or H_2O. Estimates indicate that pressure broadening could cause up to a 5% reduction from the Doppler peak absorption cross section at the highest pressure. Due to the lack of experimental information on the pressure broadening parameters in the system, this estimate was simply added to the uncertainty in the line strength determination. Thus the total absolute uncertainty in determining the [OH] was estimated to be ±15%.

As is evident from the RCF factor analysis for the CN and OH radicals, illustrated in Figures 6 and 7, respectively, reaction R1 dominated the removal of CN and OH for the first 3 ms. For the CN radical the next most important removal process

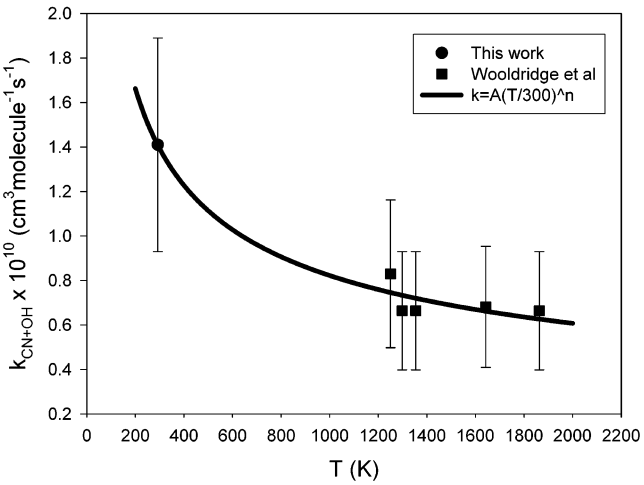

Figure 8. Available measurements for k_{R1}, (●) this work and (■) Wooldridge et al.,[4] are shown as a function of temperature. The solid line, —, is a weighted fit to the data points to give $k_{R1} = 1.39 \times 10^{-10}(300/T)^{0.437}$. The error bars are an estimate of systematic and random errors for each experiment.

was reaction with a background impurity, k_{first}^{CN}. As discussed in section III.B, k_{first}^{CN} was measured by replacing the N_2O flow by Ar and recording the removal rate constant for CN. As long as no other impurity was introduced in the N_2O flow, this procedure determined k_{first}^{CN}. Only a single measurement of k_{first}^{CN} was made for each experimental run and an uncertainty of ±10% was assigned to it. Generally, RCF_{1st}^{CN} was found to vary from 0.18 to 0.09 with an average value of 0.16 so that the uncertainty in k_{first}^{CN} contributed about ±2% to the overall uncertainty in the determination of k_{R1}.

The computer simulations of the CN profiles were taken as the best representation of the determination of k_{R1}, and as summarized in Table 2, the average value of k_{R1} was $(1.41 \pm 0.17) \times 10^{-10}$ cm^3 molecules^{-1} s^{-1}, where the stated uncertainty was taken as the average value of the computer determined Δk_{R1} at the 68% confidence level in the fit. As is evident from Table 2, the integrated-profiles method produced very similar results. The complete error in measuring k_{R1}, including systematic and random error was estimated to be 34% so that k_{R1} is given by $(1.4 \pm 0.48) \times 10^{-10}$ cm^3 molecules^{-1} s^{-1} at a temperature of 292 ± 2 K.

B. Comparison with Previous Measurements. As noted in the Introduction, the only previous direct measurement of k_{R1} has been the shock tube experiments by Wooldridge et al.[4] These workers simultaneously monitored CN and OH using time-resolved UV absorption spectroscopy. The low-temperature measurement of this work and high-temperature measurements of Wooldridge et al. are shown as a function of temperature in Figure 8. The solid line in Figure 8 is a weighted nonlinear least-squares fit to all the data of the form $k_{R1} = A(300/T)^n$. The values of the fitted parameters were found to be $A = (1.39 \pm 0.3) \times 10^{-10}$ and $n = 0.437 \pm 0.26$, with uncertainties of $\pm 1\sigma$.

C. Comparison with Related Systems. Using collision cross sections of similar stable molecules, a hard sphere collision rate between CN and OH can be estimated to be about 2.6×10^{-10} cm^3 molecules^{-1} s^{-1} at 292 K. Thus at room temperature, 55% of the hard sphere collisions between CN and OH lead to reaction. This large reaction rate constant might imply that all spin and electronic manifolds participate in the reaction to some extent. In C_s symmetry there are singlet and triplet spin manifolds of A′ and A″ electronic symmetry correlating to the $CN(X^2\Sigma)$ and $OH(X^2\Pi)$ reagents.

Adiabatically, at least 75% of the collisions between CN and OH occur in the triplet spin manifold so that the lowest energetic triplet potential energy surface, ^{3}A′, is expected to make the largest contribution to reactive collisions. Although there have been a large number of theoretical calculations on the H, C, N, O system, almost all of these studies have been carried out to understand the photochemistry and photophysics of isocyanic acid, HNCO. However, Mebel et al.[44] have investigated the lowest energetic global A′ PES of the HCNO system in both the singlet and triplet spin manifolds. These calculations were carried out using the hybrid density functional B3LYP method with a 6-311G(d,p) basis set. Although the energetics of these calculations are expected to be accurate to within 20−40 kJ mol^{-1}, the calculations provide a good representation of the global features of the PES and provide a qualitative understanding of the collision dynamics. As far as k_{R1} is concerned, the calculations show that CN and OH can approach on a barrierless ^{3}A′ PES to form a triplet cyanic acid (HOCN) intermediate, in either cis or trans configurations, and dissociate to form the $H(^2S) + NCO(X^2\Pi)$ product channel through a transition state 64 kJ mol^{-1} below the CN + OH reactant asymptote. Similarly, on the lowest energy ^{1}A′ PES, the reactants can form singlet cyanic acid (HOCN, ^{1}A′) without a barrier, and decompose, again over a barrierless PES into the $H(^2S) + NCO(X^2\Pi)$ product channel. On this ^{1}A′ PES, the product, H + NCO asymptote was calculated to be 172 kJ mol^{-1} lower in energy than the reactant asymptote. Thus, on the lowest energetic ^{1}A′ and ^{3}A′ PES's, the CN and OH radicals can interact over attractive PESs to form an HOCN adduct, which can decompose exothermically to the H + NCO product channel.

The topology of the next energetic singlet PES, ^{1}A″, has not been studied globally but should have the same general characteristics as the ^{3}A″ state, except to lie at higher energies than the triplet surface. Both PES's arise from the same, A″, electronic configuration but differ in electron spin alignment. Indeed, the theoretical calculations on the isomer, isocyanic acid, HNCO, indicate that this is the case.[45] Thus, it might be speculated that the initial interaction between CN and OH occurring on the ^{1}A″ PES will also be attractive, leading to reactive encounters on this PES. However, calculations[45] show that in HNCO rapid intersystem crossing can occur, and it is likely to be important in HOCN as well.

There are no guidelines as to the general shape for the next energetic triplet PES, ^{3}A′, for HOCN. The ^{3}A′ PES arises from internal excitation of an electron in a $(9a')^2$ molecular orbital to a more energetic unoccupied (10a′) orbital. For HNCO, calculations[46] show that motions leading from wells on the ^{3}A′ PES to the various product channels all pass through transition states with energies above the respective product asymptotes so that the reverse motions are all repulsive in nature. There is no information about the CN + OH interaction on the ^{3}A′ PES. For HNCO the ^{3}A′ PES participates in the photodissociation dynamics through internal conversion and intersystem crossing.[45,46]

Although the systematic and random errors are large for k_{R1}, the temperature dependence is close to $(1/T)^{0.5}$. Both the $CN(^2\Sigma) + O_2(^3\Sigma)$ and $NCO(^2\Pi) + O(^3P)$ reactions have rate constants with similar $(1/T)^{0.5}$ temperature dependencies.[5,47] All three reactions are examples of radical−radical reactions, involving predominantly C, N, and O atoms. Each reaction is characterized by having two spin manifolds, doublet-quartet, singlet−triplet, and doublet-quartet, but different numbers of

electronic manifolds in C_s symmetry, A″, (A′ + A″), and 3(A′ + A″) for CN + O_2, CN + OH, and NCO + O, respectively. For all three systems, at least one of the potential energy surfaces is attractive; i.e., there is no appreciable energy for the reactants to pass over a relatively deep potential well before proceeding on to products. Indeed, for the CN + O_2 reaction detailed theoretical calculations using a description of the initial attractive interaction based on an ab initio calculation and variational statistical calculation of the complex rate constant were able to rationalize the unique temperature dependence of this reaction.[5,48] Both the magnitude and temperature dependence of the calculated rate constant were in reasonable agreement with experiment.

V. Conclusion

The rate constant for the radical−radical reaction, CN($^2\Sigma$) + OH($^2\Pi$), was determined both directly, by applying the integrated-profiles method to experimentally determined CN and OH temporal concentration profiles, and indirectly, by varying k_{R1} in a detailed kinetic model until agreement was found between the experimental and calculated CN temporal profiles. The two methods gave very similar values for k_{R1}. The best estimate of k_{R1} was taken as that determined using the kinetic model, and gave $k_{R1} = (1.4 \pm 0.48) \times 10^{-10}$ cm^3 molecule^{-1} s^{-1}, where the uncertainty reflects both systematic and random error, at a temperature of 292 ± 2 K.

The comparison between the integrated-profile method and the chemical model analysis demonstrates that the integrated-profile method can be a powerful tool in the direct determination of radical−radical rate constants.

Acknowledgment. This work was supported by the U.S. Department of Energy, Office of Basic Energy Sciences, Division of Chemical Sciences, Geosciences, and Biosciences, under contract No. W-31-109-ENG-38

References and Notes

(1) Warnatz, J.; Maas, U.; Dibble, R. W. *Combustion: Physical and Chemical Fundamentals, Modeling and Simulation, Experiments, Pollution Formation*; Springer: Berlin, 1995.
(2) Dean, A. M.; Bozzelli, J. W. In *Gas-Phase Combustion Chemistry*; Gardiner, Jr., W. C., Ed.; Springer: New York, 1999.
(3) Miller, J. A.; Bowman, C. T. *Prog. Energy Combust. Sci.* **1989**, *287*, 1989.
(4) Wooldridge, S. T.; Hanson, R. K.; Bowman, C. T. *Int. J. Chem. Kinet.* **1996**, *28*, 245.
(5) Smith, I. W. M. *The Chemical Dynamics and Kinetics of Small Radicals, Part 1*; Liu, K., Wagner, A., Eds.; World Scientific: Singapore, 1995.
(6) Ruscic, B.; Feller, D.; Dixon, D. A.; Peterson, K. A.; Harding, K. B.; Asher, R. L.; Wagner, A. F. *J. Phys. Chem. A* **2001**, *105*, 1.
(7) Lee, T. J.; Rendell, A. P. *Chem. Phys. Lett.* **1991**, *177*, 491.
(8) Rinnenthal, J. L.; Gericke, K. H. *J. Mol. Spectrosc.* **1999**, *198*, 115.
(9) Zyrianov, M.; Droz-Georget, Th.; Sanov, A.; Reisler, H. *J. Chem. Phys.* **1996**, *105*, 8111.
(10) Laidler, K. J. *Chemical Kinetics*; McGraw-Hill: New York, 1965.
(11) Yamasaki, K.; Watanabe, A. *Bull. Chem. Soc. Jpn.*. **1997**, *70*, 89.
(12) Yamasaki, K.; Watanabe, A.; Kakuda, T.; Tokue, I. *Int. J. Chem. Kinet.* **1998**, *30*, 47.
(13) He, G.; Tokue, I.; Harding, L.; Macdonald, R. G. *J. Phys. Chem. A* **1998**, *102*, 7653.
(14) Kroto, H. W. *Molecular Rotational Spectra*; Dover: New York; 1992.
(15) Bethardy, G. A.; Macdonald, R. G. *J. Chem. Phys.* **1995**, *103*, 2863.
(16) Atkinson, R.; Baulch, D. L.; Cox, R. A.; Hampson, Jr., R. F.; Kerr, J. A.; Troe, J. *J. Phys. Chem. Ref. Data* **1992**, *21*, 1992.
(17) Davidson, J. A.; Schiff, H. I.; Brown, T. J.; Streit, G. E.; Howard, C. J. *J. Chem. Phys.* **1978**, *69*, 1213.
(18) Tsang, W. *J. Chem. Ref. Data* **1992**, *21*, 753.
(19) Titarchuk, T. A.; Halpern, J. B. *Chem. Phys. Lett*. **1995**, *232*, 192.
(20) Sims, I. R.; Smith, W. M. *Chem. Phys. Lett.* **1988**, *149*, 565.
(21) Rim, K. T.; Hershberger, J. F. *J. Phys. Chem. A* **1999**, *103*, 3721.
(22) Jacobs, A.; Wahl, M.; Weller, R.; Wolfrum, J. *Chem. Phys. Lett.* **1988**, *144*, 203.
(23) Williams, B. A.; Papas, P.; Nelson, H. H. *J. Phys. Chem.* **1995**, *99*, 13471.
(24) Baulch, D. L.; Cobos, C. J.; Cox, R. A.; Esser, C.; Frank, P.; Just, Th.; Kerr, J. A.; Pilling, M. J.; Troe, J.; Walker, R. W.; Warnatz, J. *J. Phys. Chem. Ref. Data* **1992**, *21*, 411.
(25) Smith, I. W. M.; Stewart, D. W. A. *J. Chem. Soc., Faraday Trans.* **1994**, *90*, 3221.
(26) Miller, J. A.; Bowman, C. T. *Int. J. Chem. Kinet.* **1991**, *23*, 289.
(27) Bedjanian, Y.; Bras, G. Le.; Poulet, G. *J. Phys. Chem. A* **1999**, *103*, 7017.
(28) Zellner, R.; Ewig, F.; Paschke, R.; Wagner, G. *J. Phys. Chem.* **1988**, *92*, 4184.
(29) Knowels, P. J.; Werner, H.-J.; Cartwright, D. C. *J. Chem. Phys.* **1988**, *89*, 7334.
(30) He, G.; Tokue, I.; Macdonald, R. G. *J. Chem. Phys.* **1998**, *109*, 6312.
(31) Nelson, Jr. D. D.; Schiffman, A.; Nesbitt, D. J.; Orlando, J. J.; Burkholder, J. B. *J. Chem. Phys.* **1990**, *93*, 7003.
(32) North, S. W.; Hall, G. E. *J. Chem. Phys.* **1997**, *106*, 60.
(33) Sauder, D. G.; Stephenson, J. C.; King, D. S.; Casassa, M. P. *J. Chem. Phys.* **1992**, *97*, 952.
(34) Tanaka, N.; Takayanagi, M.; Hanazaki, I. *Chem. Phys. Lett.* **1996**, *254*, 40.
(35) Bethardy, G. A.; Northrup, F. J.; He, G.; Tokue, I.; Macdonald, R. G. *J. Chem. Phys.* **1998**, *109*, 4224.
(36) Decker, B. K.; Macdonald R. G. Manuscript in preparation.
(37) Yang, D. L.; Lin, M. C. In *The Chemical Dynamics and Kinetics of Small Radicals, Part I*; Liu, K., Wagner, A., Eds.; World Scientific: Singapore, 1995.
(38) Cohen, N.; Westberg, K. R. *J. Chem. Ref. Data* **1991**, *20*, 1211.
(39) Phillips, L. F. *Combust. Flame* **1979**, *35*, 233.
(40) Harding, L. B.; Wagner, A. F. *22nd International Symposium on Combustion*; The Combustion Institute: Pittsburgh, 1988; p 983.
(41) DeMore, W. B.; Sander, S. P.; Golden, D. M.; Hampson, R. F.; Kurylo, M. J.; Howard, C. J.; Ravishankara, A. R.; Kolb, C. E.; Molina, M. J. *Chemical Kinetics and Photochemical Data for Use in Stratospheric Modeling;* JPL Publication 97-4; Pasadena, CA, 1997.
(42) Earls, L. T. *Phys. Rev.* **1935**, *48*, 423.
(43) Rothman, L. S.; Rinsland, C. P.; Goldman, A.; Massie, S. T.; Edwards, D. P.; Flaud, J.-M.; Perrin, A.; Camy-Peyret, C.; Dana, V.; Mandin, J.-Y.; Schroeder, J.; Mccann, A.; Gamache, R. R.; Wattson, R. B.; Yoshino, K.; Chance, K. V.; Jucks, K. W.; Brown, L. R.; Nemtchinov, V.; Varanasi, P. *J. Quant. Spectrosc. Radiat. Transfer* **1998**, *60*, 665.
(44) Mebel, A. M.; Luna, A.; Lin, M. C.; Morokuma, K. *J. Chem. Phys.* **1996**, *105*, 6439.
(45) Kaledin, A. L.; Cui, Q.; Heaven, M. C.; Morokuma, K. *J. Chem. Phys. A* **1999**, *111*, 5004.
(46) Valeev, E. F.; Allen, W. D.; Schaefer, H. F., III; Csaszar, A. G.; East, A. L. L. *J. Phys. Chem. A* **2001**, *105*, 2716.
(47) Gao, Y.; Macdonald, R. G. *J. Phys. Chem. A* **2003**, *107*, 4625.
(48) Klippenstein, S. J.; Kim, Y.-W. *J. Chem. Phys.* **1993**, *99*, 5790.